




Article

# Three-Degree-of-Freedom Cable-Driven Parallel Manipulator with Self-Sensing Nitinol Actuators

Francesco Durante <sup>1,\*</sup> , Terenziano Raparelli <sup>2</sup>  and Pierluigi Beomonte Zobel <sup>1</sup> 

<sup>1</sup> Department of Industrial and Information Engineering and Economy (DIIIE), University of L'Aquila, P.le Pontieri 1, Località Monteluco, 67100 L'Aquila, Italy; pierluigi.zobel@univaq.it

<sup>2</sup> Department of Mechanical and Aerospace Engineering (DIMEAS), Politecnico di Torino, Corso Duca degli Abruzzi 24, 10129 Torino, Italy; terenziano.raparelli@polito.it

\* Correspondence: francesco.durante@univaq.it

**Abstract:** This paper presents the design and analysis of a novel 3-degree-of-freedom (3-DOF) parallel manipulator equipped with self-sensing Ni-Ti (Nitinol) actuators. The manipulator's architecture and mechanical design are elucidated, emphasizing the integration of Nitinol actuators. The self-sensing technique implemented in a previous work was extended to a 20 mm actuator length, and the actuator was used to design the 3-DOF manipulator. Kinematic analyses were conducted to evaluate the manipulator's performance under various operating conditions. A dynamic model was implemented for the dynamic dimensioning of the actuators, which work synergistically with a bias spring. The manipulator was realized, and a control strategy was implemented. Experimental tests, although documenting some positioning accuracy issues, show the efficacy and potential applications of the proposed manipulator in robotics and automation systems, highlighting the advantages of self-sensing Nitinol actuators in small parallel manipulator designs.

**Keywords:** parallel manipulator; Ni-Ti actuators; kinematic analysis; dynamic analysis; robotics; cable robot



**Citation:** Durante, F.; Raparelli, T.; Beomonte Zobel, P. Three-Degree-of-Freedom Cable-Driven Parallel Manipulator with Self-Sensing Nitinol Actuators. *Robotics* **2024**, *13*, 93. <https://doi.org/10.3390/robotics13060093>

Academic Editors: Swaminath Venkateswaran and Jong-Hyeon Park

Received: 28 May 2024

Revised: 17 June 2024

Accepted: 18 June 2024

Published: 20 June 2024



**Copyright:** © 2024 by the authors. Licensee MDPI, Basel, Switzerland. This article is an open access article distributed under the terms and conditions of the Creative Commons Attribution (CC BY) license (<https://creativecommons.org/licenses/by/4.0/>).

## 1. Introduction

Parallel manipulators have gained significant attention in robotics due to advantages such as high rigidity, accuracy, and payload capacity. In recent years, there has been a growing interest in integrating smart materials, particularly shape memory alloys (SMAs), into robotic systems to enhance their performance and capabilities. Among SMAs, nickel–titanium (Ni-Ti) alloys stand out for their unique properties, including high energy density, biocompatibility, and shape memory effect, making them ideal candidates as actuators [1–6] in many applications in different fields, such as in aerospace [7–11], biomedicine [12–17], wearables [18–21], micro-systems [22–25], and robotics [26–32]. There are not many works in the literature regarding manipulators with parallel architecture with SMA actuators. In [33], a parallel device for the orientation of the platform connected to the base via a flexible central rod in superelastic Nitinol is described. Three Nitinol wires arranged at 120° are used as actuators. The flexible structure reflects a system with two DOFs. The dimensions are contained in a cylinder of 65 mm in diameter and 75 mm in height. For the movement, a structural model allows position control through the knowledge of the forces applied by the actuators, which are detected using force sensors on each actuator. The experimental tests were carried out with the movement of just one actuator, and the authors also plan to use a position detection system. Ref. [34] describes a parallel manipulator that uses actuators made by a carriage on a slide connected to an elastic plate that is bent by the actuator and shortens. The wires are kept in an eccentric configuration concerning the plate to amplify the shortening. Control is implemented with on–off commands based on feedback using a signal from linear variable displacement transducers (LVDTs), one for each actuator. The system has three DOFs and good performance. Still,

it is rather large, given that the actuators are bulky in order to achieve the amplification effect, i.e., they have a length of approximately 220 mm and a transversal dimension of roughly 40 mm × 50 mm. The device is contained in a cylinder with a diameter of 230 mm and a height greater than 220 mm. In [35], the device BAPAMAN is presented. It is a module comprising a base and a platform connected by three legs arranged at 120°. Each includes two articulated segments, and all the connections between the two segments of the leg and between the leg with the base and platform are made using flexible joints. There is a cylindrical hinge between the leg and the base and between the leg segments, while there is a universal joint between the leg and the platform. The platform has five DOFs with respect to the base: three translational and two rotational. The system is designed to be organized into multiple serial modules to constitute a snake robot instead of a parallel manipulator. As for the movements, they are implemented in binary mode. Each leg features two actuators, giving the module eight different configurations. The overall dimensions of the single module are contained in a cylinder with a diameter of 180 mm and a height of 200 mm. In [36], a parallel manipulator with a square base and a platform that implements four SMA springs arranged at the vertices as actuators, each with a steel antagonist spring, is presented. The movements are implemented in binary mode. It features three DOFs for roll pitch and one along the vertical axis. The system has small dimensions, 30 mm × 30 mm × 34 mm, and performs large movements: a rotation of the platform of 30° and a stroke in the vertical direction of 12 mm, thanks to the high deformation of the SMA springs. Given the structure, it is probably not very rigid, losing a peculiar characteristic of parallel architecture robots. The biggest limit, however, is the actuators' binary operation, which leads to a limited number of possible configurations, placing the end effector discreetly in the working volume. Reference [37] describes a system with a triangular base and platform connected with a universal joint and SMA springs at the vertices. It features two DOFs: pitch and roll. The dimensions are contained in a cylinder with a diameter of 92 mm and a height of 114 mm. A position control with an on-off type command in the closed loop is implemented using an IMU sensor. In [38], a 3-DOF parallel manipulator with SMA wire actuators is presented. It features a base and a platform. The base and platform are connected to the actuators, which are constantly tensioned by a bias spring between the base and the platform. The manipulator implements proportional position closed-loop control, using the signal generated by a potentiometer for each actuator. The project functions well, but the system is rather bulky, given the presence of position sensors. The dimensions are contained in a cylinder with a diameter of 82 mm and a height of approximately 210 mm.

This paper presents the design and analysis of a novel 3-DOF parallel manipulator utilizing self-sensing Ni-Ti actuators. Integrating self-sensing capabilities within the actuation system eliminates the need for external sensors, simplifies the overall design, and reduces the system's complexity, size, and cost. Also, using Ni-Ti actuators allows for smooth and silent actuation mechanisms. The proposed parallel manipulator is compact and lightweight. It suits various tasks requiring the positioning and manipulation of small objects, such as pick-and-place operations, assembly tasks, and biomedical applications. The paper describes the design methodology, i.e., kinematic modeling and analysis of the manipulator's workspace, singularity conditions, error analysis, and dynamic modeling for the actuation system dimensioning of the proposed 3-DOF parallel manipulator and the investigation of dynamic performance characteristics, including integrating self-sensing Ni-Ti actuators. Furthermore, the experimental validation of the realized manipulator prototype is conducted to assess its performance for positional accuracy. The results, except for a limited area of the working volume in which positioning errors outside the expected range occur, prove the effectiveness of the project by demonstrating that for the creation of cable-driven manipulators, it is possible to use self-sensing shape memory alloy wires exploiting their self-sensing characteristic, thus allowing compact dimensions to be obtained. Compared to the devices in the scientific literature, the proposed manipulator is similar to

the one described last. A comparison with that manipulator has been conducted to prove the actual project's performance.

The contents of the paper are organized as described below. In Section 2, Materials and Methods, the mechanical design of the manipulator is reported (Section 2.1), it is addressed through the technical specification and functional design (Section 2.1.1), and then continues with the characterization of the Ni-Ti actuator (Section 2.1.2). Following these are the forward kinematic analysis (Section 2.1.3), the inverse kinematic analysis (Section 2.1.4), and the differential kinematic analysis (Section 2.1.5). The next section contains a dynamic analysis to verify the sizing of the actuator and spring system (Section 2.1.6). Then, the next subsection (Section 2.1.7) describes the detailed project. Subsequently, in Section 2.2, the control is described with regard to the hardware (Section 2.2.1) and the control strategy (Section 2.2.2). In Section 3, the results are presented. Section 3.1 presents the results relating to the estimation of the error on the working volume boundaries based on the errors detected on the single actuator. Subsequently, the prototype of the manipulator is presented (Section 3.2), and subsequently, the results of the positioning tests relate to the movement of the individual actuators and tests for trajectory tracking (Section 3.3). In Section 4, a discussion of the results is carried out, possible future developments are proposed, a comparison is made between the proposed system and a similar one, and conclusions are drawn.

## 2. Materials and Methods

### 2.1. Mechanical Design of the Manipulator

#### 2.1.1. Manipulator's Technical Specification and Functional Design

The manipulator has to serve as a proof of concept for a small manipulator with parallel architecture, using shape memory alloy wires as actuators. Taking as a reference a Stewart platform, some preliminary analyses suggest that it is convenient to consider technical specifications for the design of the device, as follows:

- Number of DOFs: 3 without wrist and gripper;
- Overall dimensions, including actuators, contained in a cylinder with a diameter of 45 mm and a height of 140 mm;
- Diameter of the circle circumscribed to the plan projection of the working volume by height, in the range of 10 mm  $\times$  2 mm;
- Actuator's block control volume not more than 20,000 mm<sup>3</sup>;
- Overall mass without the electronics for control of not more than 0.05 kg;
- The manipulator is intended to manipulate tiny mass objects, so the considered load capability is 0.05 N.

Following the specifications above, the kinematic architecture of Landsberger's robot is considered [39]. A system consisting of a base and a platform, with the dimensions of the platform reduced to zero, is considered according to the scheme in Figure 1 [40].

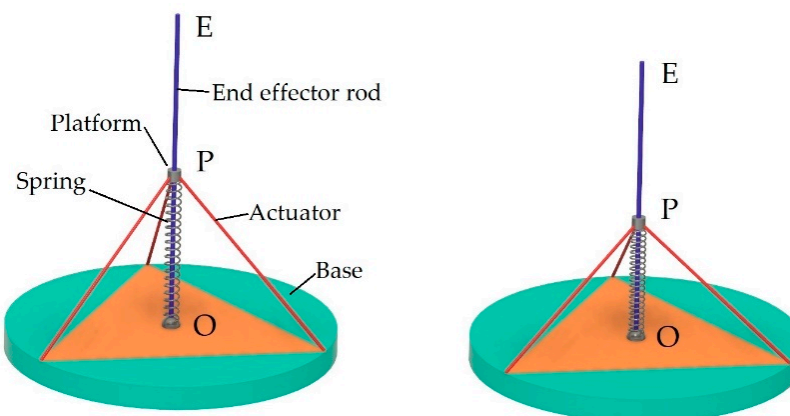


Figure 1. Concept of the manipulator.

The proposed idea is to implement Ni-Ti wires as actuators using the self-sensing effect. This way, it is possible to eliminate motors, drums, and external sensors, thus avoiding an increase in overall dimensions. The actuators are anchored to the base, each to the three vertices of an equilateral triangle, and on the other side to the platform, which is a tiny body. The actuators, which work only by traction, are constantly tensioned thanks to a compressed bias spring placed between the central point of the base, O, and the point P, representing the platform.

To amplify the movements, a small rod is used, which is coupled to the base via a joint consisting of a sphere articulated on the base and drilled to accommodate the end of the rod in a prismatic coupling. This joint allows the rod to rotate and slide along the direction of its axis relative to the base. At the other end, the rod is integral to the platform, P, and extends beyond it. The upper end of the rod, E, is at a fixed distance from the platform; it constitutes the end effector of the manipulator to which a tool can be applied.

### 2.1.2. Characterization of Actuators Using Self-Sensing Effect

Based on preliminary evaluations of the hypothesized architecture, a system with actuators approximately 20 mm long can satisfy the technical specification. The work [41] demonstrated that a Ni-Ti wire can work well as an actuator with a self-sensing effect. In that work, the effectiveness of a wire with a length of 200 mm was demonstrated. Here, the hypothesis is to work with a much shorter actuator. Therefore, before proceeding with the design of the manipulator, it is necessary to experimentally verify the effectiveness of the self-sensing process on a wire with a length of 20 mm.

The same Ni-Ti wire whose characteristics are detailed in Table 1 was considered, and the same experimental setup described in [41] was used but with a modification of the index of the graduated scale, which was brought to a greater length to amplify the movement generated by the actuator for better visualization. In this case, the actuator will have a total excursion equal to approximately 0.7 mm, considering a percentage shortening of 3.5%, so length variations of a hundredth of a mm must be detectable. Changes have been made to the electrical components of the control system to adapt them to the different electrical parameters of the shorter wire. The electrical measurement resistance was brought to 3.9 Ohm and the supply voltage to 1.1 V.

**Table 1.** Technical specification of the wire.

<b>Flexinol 150HT</b>
Wire diameter: 150 $\mu\text{m}$
Linear resistance: 50 $\Omega/\text{m}$
Maximum recovery force: 10.4 N
Nominal recovery force: 3.2 N
Deformation force: 0.6 N
Recommended deformation ratio: 3–5%
Austenite start temperature: 88 $^{\circ}\text{C}$
Austenite finish temperature: 98 $^{\circ}\text{C}$
Martensite start temperature: 72 $^{\circ}\text{C}$
Martensite finish temperature: 62 $^{\circ}\text{C}$

Tests were conducted to characterize the wire's unitary deformation ( $\epsilon$ ) relationship with electrical resistance (R) to obtain the model for self-sensing implementation. In particular, the model was obtained for the actuator in an antagonistic configuration with a bias spring. The resulting model was represented as a linear one

$$\epsilon = 26.374 - 17.419 R \quad (1)$$

whose relative graph is shown in Figure 2.

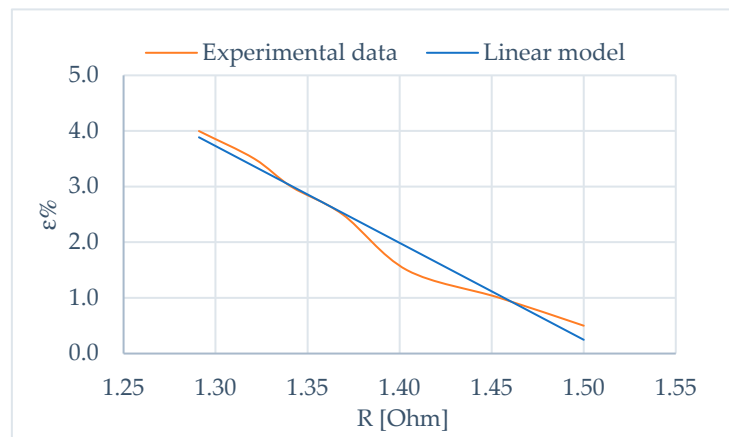


**Figure 2.** A linear mathematical model for the electrical resistance deformation for the NiTi alloy wires is adopted for the control.

Positioning tests were conducted using the model and the setup described. A precision potentiometer connected to the pulley [41] was added to acquire the actual position using a data acquisition board. It turns out that the actuator works well over the entire operating range (0.7 mm), except for the value close to the minimum length, i.e., for an elongation equal to 0.1 mm. Figure 3 shows the system responses for stepped input signals. There is an error due to oscillations of approximately 0.04 mm.

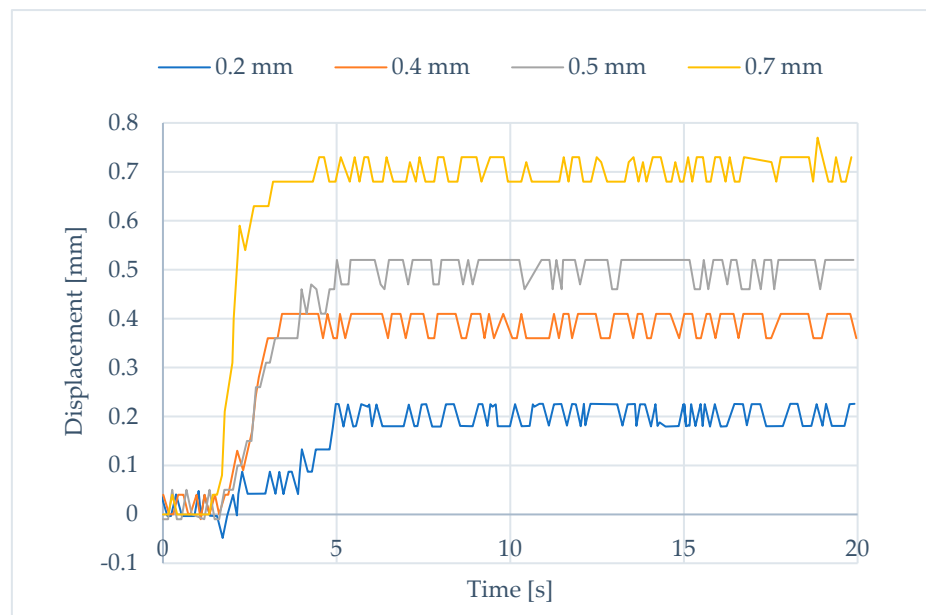


**Figure 3.** Responses of the 20 mm long actuator with the self-sensing process to step inputs of 0.2 mm, 0.4 mm, 0.5 mm, and 0.7 mm. The responses are quick with a precise mean value, but oscillations occur with an amplitude of less than 0.02 mm.

### 2.1.3. Direct Kinematic Model—Domain Analysis

For the working volume analysis, the direct kinematic model was considered. With reference to Figure 4, we name  $O_1$ ,  $O_2$ , and  $O_3$  as the three points at which the actuators are attached to the base, with each at a distance  $b$  from the center of the base,  $O$ . A fixed frame attached to the base is considered, such that the origin is located at the center of the base, with the  $x$ -axis pointing toward the point  $O_1$ , the  $z$ -axis pointing upward, and the  $y$ -axis pointing coherently with a right-handed reference. Each actuator is represented by a vector  $l_i$  ( $i = 1, 2, 3$ ) from  $O_i$  to the point  $P$ , and all the actuators have the same initial length. The

first step in determining the direct kinematic model is to solve for the position of the point  $P$  given the values of the actuator's lengths,  $l_i$ . For each actuator, the loop closure equations can be written as

$$OP - OO_i = l_i \quad i = 1,2,3. \tag{2}$$

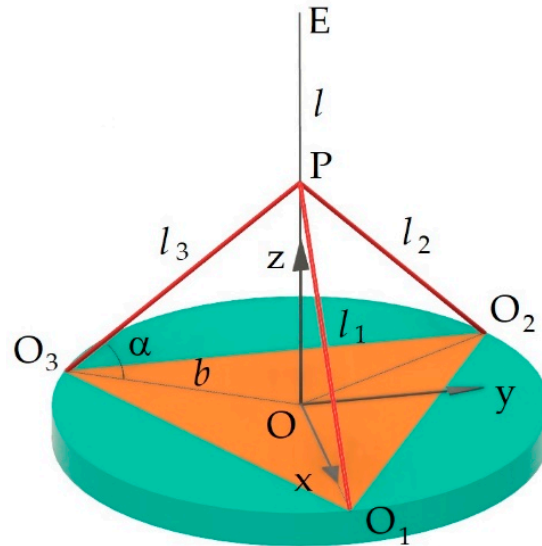


Figure 4. Parameters for the kinematic model of the manipulator.

The vector  $OP$  is as follows:

$$OP = [x_P, y_P, z_P]^T \tag{3}$$

while  $OO_i$  have a fixed magnitude and are as

$$OO_1 = [b, 0, 0]^T \tag{4}$$

$$OO_2 = \left[ -\frac{1}{2}b, \frac{\sqrt{3}}{2}b, 0 \right]^T \tag{5}$$

$$OO_3 = \left[ -\frac{1}{2}b, -\frac{\sqrt{3}}{2}b, 0 \right]^T \tag{6}$$

We can substitute Equations (3)–(6) into Equation (2), resulting in three vector equations with three unknowns, the coordinates of the point  $P$ , for a given set of  $l_i$ . Therefore, we have to solve the three equations with three unknowns simultaneously for the position of the platform (point  $P$ ) to be determined.

Before solving Equation (2), the values of the manipulator's design parameters, namely the actuators' rest length and the base's dimension  $b$ , must be defined. To do that, we can choose a resting length for the actuators and then derive the dimensions of the base from it.

The choice of these parameters derives from an optimization process between conflicting needs. In fact, for a given length of the actuators, the excursion of the end effector in the vertical direction is more extensive, and consequently, the same is true for the working volume, the smaller the angle  $\alpha$ . That involves a greater overall dimension of the basis and, therefore, a bigger value for  $b$ .

From a quantitative point of view, the distance  $OP$ , given the size of the base  $b$  and the actual length of the actuators,  $l_i$ , is

$$OP = l_i \sqrt{1 - \left(\frac{b}{l_i}\right)^2} \tag{7}$$

Once the value  $b$  has also been hypothesized, with relation (7), it is possible to calculate the distance OP, considering the variation in the actuator’s length and the end effector’s vertical excursion. Therefore, based on what has been said, we will proceed by hypothesizing different values for  $b$ , evaluating the best compromise solution between the excursion of the end effector, which we want to be large, and the overall size of the base, which we wish to be small. Table 2 shows the results for the cases relating to the actuator, with nominal length dimensions equal to 20 mm and different hypothesized values for dimension  $b$ . From the data observation, we chose to work with  $b = 16.5$  mm as it constitutes a good compromise between the base’s size and the end effector’s excursion.

**Table 2.** Parameters’ comparison for the choice of the characteristic dimension of the robot,  $b$ .

$b$ (mm)	$\alpha_M$ (°)	$\alpha_m$ (°)	OP <sub>M</sub> (mm)	OP <sub>m</sub> (mm)	$\Delta(OP)$ (mm)
10.00	60.00	58.79	17.32	16.51	0.81
11.00	56.63	55.25	16.70	15.86	0.84
12.00	53.13	51.56	16.00	15.12	0.88
13.00	49.46	47.66	15.20	14.26	0.93
14.00	45.57	43.50	14.28	13.28	1.00
15.00	41.41	38.99	13.23	12.14	1.08
16.00	36.87	34.00	12.00	10.79	1.21
16.50	34.41	31.25	11.30	10.01	1.29
17.00	31.79	28.26	10.54	9.14	1.40
18.00	25.84	21.15	8.72	6.96	1.75
19.00	18.19	10.12	6.24	3.39	2.86

Once the geometric data characterizing the actuators were defined, the direct kinematic problem for determining the working volume was solved.

By substituting (3)–(6) into Equation (2) and then applying the norm and squaring, we can obtain the following three equations:

$$\begin{cases} (x_P - b)^2 + (y_P - 0)^2 + (z_P - 0)^2 = l_1^2 \\ \left(x_P + \frac{1}{2}b\right)^2 + \left(y_P - \frac{\sqrt{3}}{2}b\right)^2 + (z_P - 0)^2 = l_2^2 \\ \left(x_P + \frac{1}{2}b\right)^2 + \left(y_P + \frac{\sqrt{3}}{2}b\right)^2 + (z_P - 0)^2 = l_3^2 \end{cases} \quad (8)$$

These were solved with Mathematica code. An equation of the 16th order of  $x_P$  was obtained:

$$a_1 \cdot x_P^{16} + a_2 \cdot x_P^{14} + a_3 \cdot x_P^{12} + a_4 \cdot x_P^{10} + a_5 \cdot x_P^8 + a_6 \cdot x_P^6 + a_7 \cdot x_P^4 + a_8 \cdot x_P^2 + a_9 = 0 \quad (9)$$

where the expressions of the coefficients  $a_i$  are omitted because of their length.

This equation is in the 16th order of  $x_P$  and leads to 16 solutions. Since the power is always even, the solution is facilitated because it is possible to solve an 8th-degree equation. Six of these solutions are coincident, while the remaining two are symmetric with respect to the  $xy$  plane. By substituting  $x_P$  into Equation (8), it is possible to calculate  $y_P$  and  $z_P$ .

The second step concerns the calculation of the coordinates of the end-effector E ( $x_E, y_E, z_E$ ). The distance OP is a function of the coordinates of the point P:

$$OP = \sqrt{x_P^2 + y_P^2 + z_P^2} \quad (10)$$

Considering the distance of the end effector E from P as  $l$ , we have

$$x_E = x_P \frac{OP + l}{OP} \quad (11)$$

$$y_E = y_P \frac{OP + l}{OP} \quad (12)$$

$$z_E = z_P \frac{OP + l}{OP} \tag{13}$$

Thus, the direct kinematic problem is solved.

A direct kinematic analysis was carried out using the model described to visualize the boundaries of the working volume. Using a Matlab code, the lengths of the actuators were made to vary systematically in sequence, and the coordinates of the end effector in physical space were calculated. The actuators' lengths varied between 19.3 mm and 20 mm, with variations of 0.035 mm for 1386 configurations. The size of the rod was considered equal to  $l = 120$  mm. Figure 5 shows the working volume.

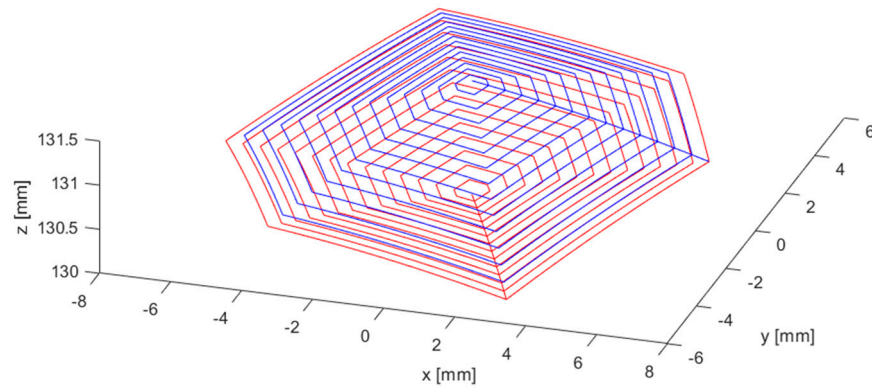


**Figure 5.** The boundaries of the working volume of the manipulator. Upper boundaries, blue; lower boundaries, red.

This resulted in a volume with a hexagonal shape in plan with an apothem equal to approximately 6 mm and with a maximum height equal to approximately 1.3 mm, as per the project.

#### 2.1.4. Inverse Kinematic Model

The inverse kinematic problem is very straightforward. Starting from a position of the end effector in the cartesian space,  $E(x_E, y_E, z_E)$ , it is possible to compute the coordinates of the point P using Equations (14)–(16):

$$x_P = x_E \frac{OE}{OE - l} \tag{14}$$

$$y_P = y_E \frac{OE}{OE - l} \tag{15}$$

$$z_P = z_E \frac{OE}{OE - l} \tag{16}$$

Then, by means of Equation (8), it is possible to solve for the coordinates in the joint space,  $l_1, l_2, l_3$ .

#### 2.1.5. Jacobian and Singularity Analysis

Starting from Equation (2), the differentiation must be carried out with respect to the time of both members. It should be considered that the derivative with respect to the time of the terms  $l_i$  has two components, one represented by the variation in length and the other by the variation in orientation with respect to the reference system of the base. However, the derivative of the segments  $OO_i$  is equal to zero since their lengths and orientations are constant. The OP vector also has two components, one due to the change in length and another due to the change in orientation (length and rotation variations of the spring with respect to the base reference). Both of these components contribute to the determination of the velocity of point P.



We find

$$\frac{d}{dt}OP - \frac{d}{dt}OO_i = \frac{d}{dt}l_i \tag{17}$$

$$\mathbf{V}_P = \dot{l}_i \mathbf{s}_i + \boldsymbol{\omega}_i \times l_i \mathbf{s}_i \tag{18}$$

where  $\mathbf{s}_i$  is the unit vector associated with the  $i$ -th actuator. To eliminate the angular velocities of actuators, we can dot-multiply both members of Equation (18) by  $\mathbf{s}_i$ . We find

$$\mathbf{s}_i \cdot \mathbf{V}_P = \dot{l}_i \mathbf{s}_i \cdot \mathbf{s}_i + \boldsymbol{\omega}_i \cdot (l_i \mathbf{s}_i \times \mathbf{s}_i) \tag{19}$$

According to [42], two Jacobians can be individuated in (19). The first one (type I Jacobian) is the coefficient of the velocity vector  $\mathbf{V}_P$ , and the other (type II Jacobian) is the coefficient of the scalar  $\dot{l}_i$

$$J_q = I \tag{20}$$

$$J_x = \begin{bmatrix} s_{1x} & s_{1y} & s_{1z} \\ s_{2x} & s_{2y} & s_{2z} \\ s_{3x} & s_{3y} & s_{3z} \end{bmatrix} \tag{21}$$

The first Jacobian can give rise to the I type of singularities. After inversion, it can be useful for calculating joint speeds to obtain the assigned speeds of the end effector. It is, therefore, similar to the Jacobian that is determined for manipulators with serial architecture, and the singularities associated with it can be defined as inverse kinematic singularities. Since, in this case, it is equal to the identity matrix, there are no singularities in the inversion. Singularities, however, occur at the edge of the working volume when the spring is at its minimum and maximum lengths.

The second one can give rise to the II type of singularities. These can occur when the end effector is locally movable, even when all the actuated joints are locked. For this reason, we can refer to them as the forward kinematic singularities.

The singularities occur when

$$\det J_x = 0 \tag{22}$$

$$s_{1x}s_{2y}s_{3z} + s_{1y}s_{2z}s_{3x} + s_{1z}s_{2x}s_{3y} - (s_{1z}s_{2y}s_{3x} + s_{1y}s_{2x}s_{3z} + s_{1x}s_{2z}s_{3y}) = 0 \tag{23}$$

The equation should then be solved. We can analyze two straightforward cases. The first occurs when all the  $z$  components of the unit vectors associated with the actuators are zero. This happens when the actuators and points  $P$  and  $E$  all lie in the plane of the base. Although theoretically possible, this condition never occurs because, in the current case, points  $P$  and  $E$  are always far from the base plane. The second occurs when the  $x$ ,  $y$ , or both components of the unit vectors associated with actuators are zero. Moreover, this is a required but not sufficient condition, since the actuators must be perpendicular to the upper base for the singularities to occur. This can be verified for an ideal architecture with a base and a platform of equal geometry. However, in the present case, where the platform is reduced to point  $P$ , the condition under the exam is never verified. The other type II singularities can also be excluded for the same reason.

### 2.1.6. Dynamic Analysis—Actuators' Dimensioning

The following applies regarding the dynamic behavior of the actuators and their interaction with the bias spring. The spring has the task of keeping the wires permanently taut. In other words, it must guarantee that the wires can recover their maximum length which requires the application of a deformation force for all the actuators simultaneously. In this sense, the most critical condition is the one in which the wire is close to its maximum length, both because the spring is in the condition of minimal compression and because the angle  $\alpha$  is at its maximum value, which involves a component of the force of the spring, useful for lengthening the wires, being smaller. At the same time, the spring has to be sufficiently soft to be compressed by the actuators in the active work phase.

Concerning Figure 6, let  $F_i$  be the force developed by the  $i$ -th actuator and  $F$  the spring force that acts along the OP direction of the rod (end effector). The following relation is valid:

$$F = \sum_i F_i \sqrt{1 - \left(\frac{b}{l_i}\right)^2} \tag{24}$$

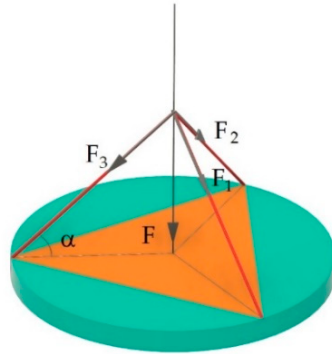


**Figure 6.** The force developed by the actuators  $F_i$  and their resultant  $F$  along the end effector rod axis. The spring has to apply a force opposite to  $F$ , as given by Equation (24).

The chosen wire for the actuators requires a low-temperature recovery force of 0.6 N and develops a high-temperature transformation force of 3.2 N.

Based on preliminary evaluations, a spring with a stiffness of  $k = 0.22$  N/mm is compatible with the bias spring utilized to obtain the actuators'  $\epsilon$ -R relationship (1). The free length of the spring is equal to 15.7 mm, and by choosing to fix its upper end on the rod below the point P at a distance equal to 3.3 mm, the force exerted by the spring, in a generic configuration, is equal to

$$F = k [15.7 - (OP - 3.3)] \tag{25}$$

A dynamic model is considered to verify the correct tensioning of the actuators by the spring over the entire working volume.

Given the actual position of point P and the force  $F$  exerted by the spring, to calculate the forces  $F_1, F_2, F_3$  exerted by the three actuators, the system equation in (26) has to be solved:

$$F_1 \frac{O_{1i} - x_i}{\sqrt{\sum(O_{1i} - x_i)^2}} + F_2 \frac{O_{2i} - x_i}{\sqrt{\sum(O_{2i} - x_i)^2}} + F_3 \frac{O_{3i} - x_i}{\sqrt{\sum(O_{3i} - x_i)^2}} = x_i \frac{F}{OP} \quad i = 1, 2, 3 \tag{26}$$

where  $x_i$  = cartesian coordinates of point P and  $O_{ji}$  = cartesian coordinates for attaching the points of the actuators to the base.

Using this model, a dynamic analysis was carried out on the entire boundary of the working volume to verify the spring. Figure 7 shows the results obtained with the dynamic model. Figure 7a shows the actuator's forces with the end effector lying on the upper working volume boundary, while Figure 7b shows the forces with the end effector lying on the lower working volume boundary, in contrast with the bias spring. The maximum spring force occurs on the lower boundary and is equal to 1.98 N, and the actuators' force has to be equal to 1.26 N for the equilibrium. Thus, since the actuators are capable of a force of 3.2 N, there is a margin to apply loads on the environment. On the upper boundary, the spring applies a minimum force of 1.69 N, and the actuators apply a minimum force of 1.22 N for the equilibrium. Since the actuators require a force of 0.6 N to be stretched at low temperatures, the spring is able to keep them taut and return them at maximum length, providing a margin to apply loads on the environment.

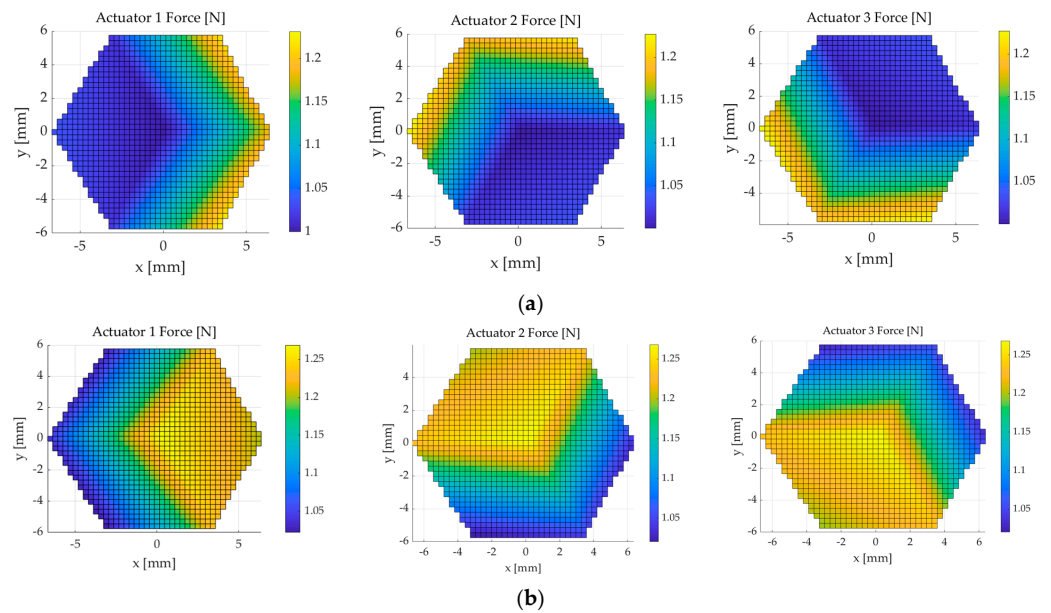


**Figure 7.** Forces applied by the actuators with the end effector lying on the upper working volume boundary (a) and lower working volume boundary (b) in contrast with the bias spring. The actuators and spring system are well-sized and succeed in the task of compressing the bias spring in every condition, while the actuators are always kept taut and stretched to their maximum length at low temperatures by the spring. In addition, excess forces result which are useful for applying loads to the environment.

2.1.7. Detailed Design

The components were designed in detail. The base is circular with a thickness of 6 mm and a diameter of 40.8 mm, and it was realized in nylon. In the center, a spherical groove is present for the articulation with the rod. The joint is realized by a spherical component with a diameter of 4.5 mm for the articulation to the base side, with a diametral hole for coupling with the rod. This one, with a diameter of 1 mm, can slide inside the hole to confer on the robot a third degree of freedom. The spherical component presents, in the upper part, a plane surface, which constitutes the base on which rests the lower extremity of the spring. The rod presents a lock for the upper extremity of the spring formed by an axisymmetric component. Above it, there is a cylindrical component for the lock of the upper extremity of the actuators. Finally, on the base, there are three holes disposed at 120° angular distance from each other, where the locks are coupled for the lower extremity of the actuators. Figure 8 shows the CAD model of the designed prototype.

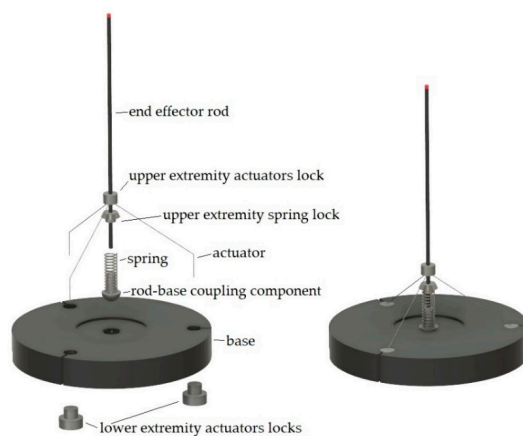


**Figure 8.** The CAD model of the manipulator.

## 2.2. Control System

In the next paragraphs, we will discuss the hardware and strategy for the control implemented.

### 2.2.1. Hardware

The hardware for the control is derived from the one used and described in [41]. The single actuator is driven by a homemade board with a drive circuit to drive the actuator and a data acquisition circuit to measure the electrical resistance to estimate its actual length. The board used for the one actuator was replicated three times on a single board to drive the three actuators to control the manipulator. Figure 9 shows the homemade drive board for the manipulator.

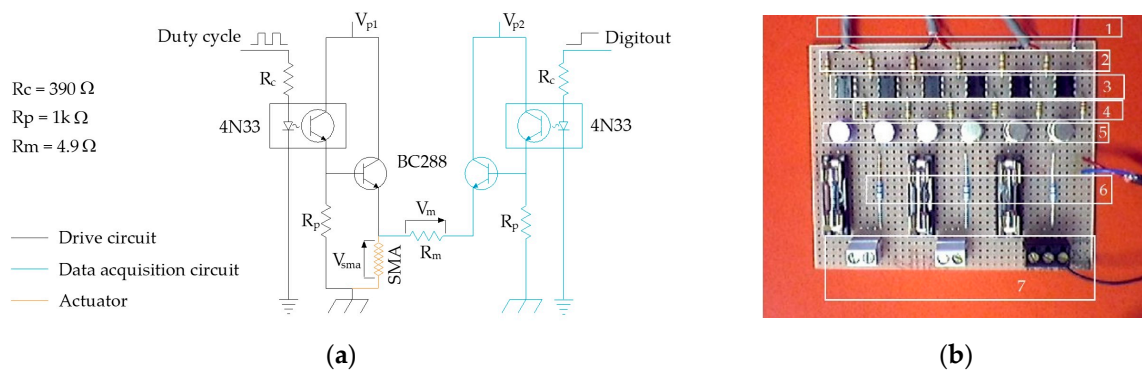


**Figure 9.** The board used for the measurement of the electrical resistance and the driving of the actuator. (a) The electric scheme; (b) the physical homemade board in which the electric scheme was replicated three times for the three actuators: (1) controller connector, (2)  $R_c$  electrical resistances, (3) 4N33 optocoupler, (4)  $R_p$  electrical resistances, (5) BC288 transistors, (6)  $R_m$  measuring electrical resistance, and (7) Ni-Ti actuators connectors.

### 2.2.2. Control Strategy

As for control, we consider the command of the actuators in one direction and rely on the bias spring for movements in the opposite direction. The law adopted applies the maximum possible value of the signal when the actuator is far from the reference and becomes proportional (P) to the error near the reference according to the law shown in Figure 10.

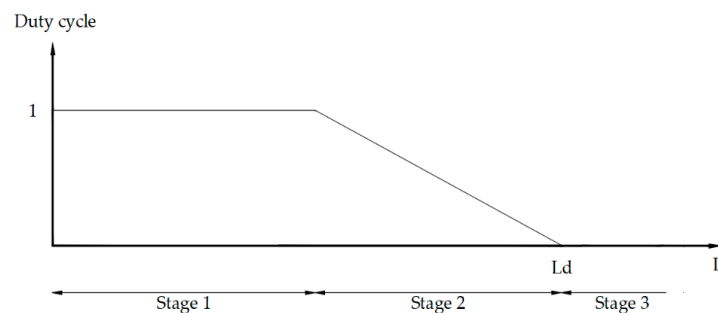


**Figure 10.** Control logic scheme: in stage 1, far from the target, the control supplies the maximum power. In stage 2, close to the target, the control becomes proportional. At stage 3, overcoming the target, the control cuts power off.

This control logic allows a faster approach phase than a purely proportional one.

The power and measurement circuits are powered alternately to estimate the actual deformation by the measurement circuit to control the actuator. This logic is adopted similarly for every one of the three actuators.

### 3. Results

#### 3.1. Analysis of the Influence of Actuator Errors on Working Volume Errors

In Figure 3, it is shown that the single actuator positioning error was about 0.02 mm. A mapping of the errors in the working volume was derived through an estimation of the influence of the errors of the three actuators using the direct kinematic model. The calculation was carried out by commanding movements equivalent to the documented errors and combining them in the worst combination of the three actuators, which corresponds to double the amplitude of the error of a single actuator. In Figure 11, the derived map is shown. It can be seen that the error is relatively constant over the working volume. The maximum values occur at three vertices where two actuators are near the maximum contraction, and a higher movement amplification effect of the cable system occurs.

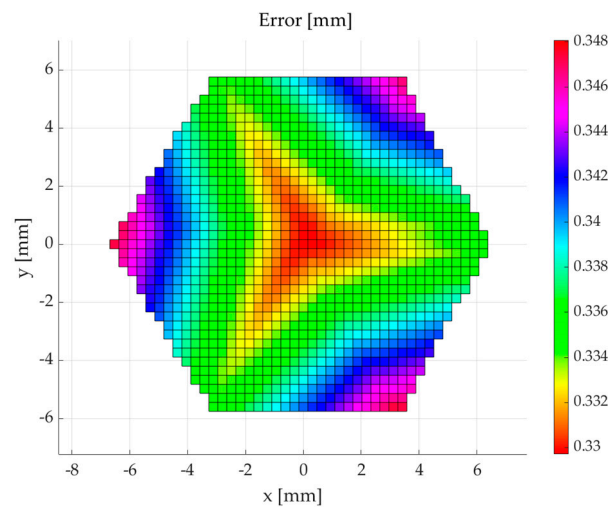


**Figure 11.** Sensitivity analysis of the error over the working volume domain due to the errors of the actuators (shown in Figure 3). It is possible to note a maximum absolute position error of 0.348 mm, corresponding to an error relative to the maximum transversal dimension of the working volume, equal to 2.7%.

#### 3.2. Manipulator Prototype

The components were realized and assembled. Particular attention had to be paid to the realization of the actuators. They have to be of the same length: 20 mm. This goal was achieved using knots and mechanical end locks realized by machining. Figure 12 shows the realized prototype.

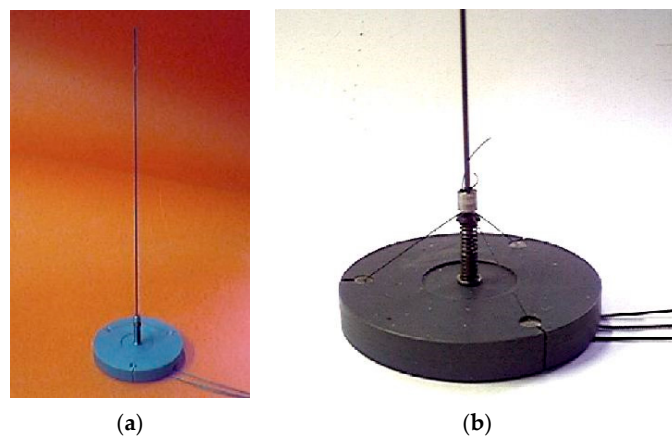


**Figure 12.** The realized prototype. An overall view showing the base and the end effector rod (a). A zoom in on the base: it is possible to see the spherical joint between the end effector and the base, as well as the spring and the NiTi wires (b).

### 3.3. Experimental Tests

The first experimental tests were about movement, involving one actuator at a time. Using lateral photography at a distance of about 4 m, it was possible to document the movements of the end effector on a graduated scale. The possibility of positioning by a single actuator one at a time was verified on the overall range of motion. Figure 13 shows the manipulator executing a single actuator movement (a) and the movement to the position (2, 0, 131.3) as viewed by the camera with the optic axis intersecting the z-axis and pointing toward the positive direction of the y-axis (b).

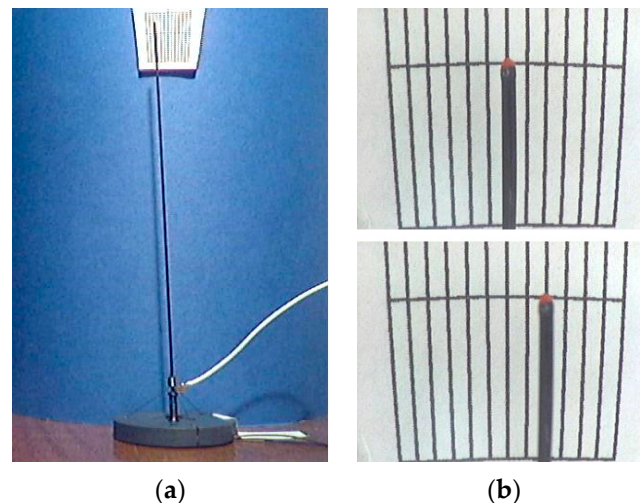


**Figure 13.** The first experimental tests were related to the positioning of an actuator at the time. A calibrated index indicates the actual position on a graduated scale where every notch corresponds to 1 mm (a). The positioning from the resting position to 2 mm (b).

Once the functionality of the single actuators was demonstrated, some tests were conducted involving coordination between the actuators in trajectory control tasks. The first involved the end effector in describing a hexagonal trajectory centered on the working volume. Subsequently, trajectories arranged without particular symmetries with respect to the working volume were tested.

As for the measurement of the movements, a camera was placed above the robot, with its optical axis pointing downward and coincident with the manipulator's vertical axis. Video of the movement was recorded for every test. Subsequently, keyframes were extracted from the videos and analyzed in a CAD environment. To have a reference for the evaluations, a paper screen with a hexagonal hole, through which the robot's end effector can be seen, was placed and centered with the vertical axis of the system and in the horizontal plane in which the motion of point E is expected to lie. Using this setup, only trajectories in the horizontal planes can be analyzed. Therefore, for a more complete characterization, there is a need for a more sophisticated setup and procedure to detect trajectories in planes different from the horizontal or with evolutions in tridimensional space.

The first trajectory tracking tests were related to hexagon trajectories centered on the working volume. Then, trajectories with less symmetry with respect to the working volume were considered as references. These described triangles whose vertices were chosen without particular conditions.

Figure 14 compares the reference trajectories and the achieved movements relating to representative cases of the tests described. Figure 14a presents the test relative to a hexagon trajectory tracking. Starting from the resting position with the end effector in (0, 0, 131.3), the trajectory reference was commanded to reach the vertices through its own coordinates in the following sequence: (−2, −3.6, 130.7), (−4, 0, 130.7), (−2, 3.6, 130.7), (2, 3.6, 130.7), (4, 0, 130.7), (2, −3.6, 130.7), (−2, −3.6, 130.7); the comparison is made by 23 points of the actual trajectory. Figure 14b presents the test relative to triangular trajectory tracking.

Starting from the resting position with the end effector in (0, 0, 131.3), the trajectory was commanded to reach the vertices through the own coordinates in the following sequence: (-0.3, -2, 130.7), (-4, 1.7, 130.7), (3.4, 1, 130.7); the comparison is made by 13 points of the actual trajectory.

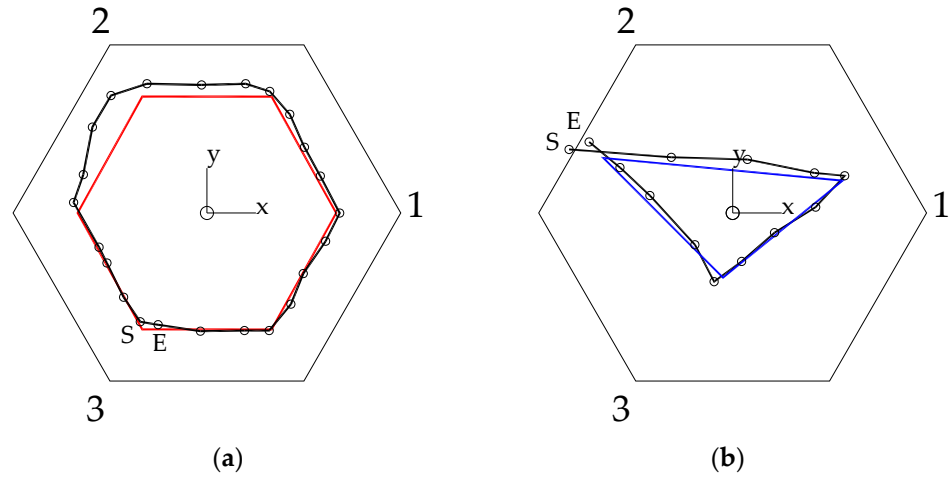


**Figure 14.** Trajectory tracking tests. The numbers 1, 2, and 3 represent the directions through which the action of the corresponding actuator moves. The letters S and E represent the trajectory’s start and end positions. The circles represent the points of the actual trajectory. (a) Representative case of the first trajectory-tracking test: the reference (red line) is an almost regular hexagon with an edge of 4 mm. (b) Representative case of the second trajectory-tracking test: the reference is a general triangle (blue line).

Figure 15 shows the errors of the trajectory tracking tests computed by the distance between the achieved positions, i.e., the black circles, and the reference trajectories, with the red line, and the blue line for the relative tests documented in Figure 14.

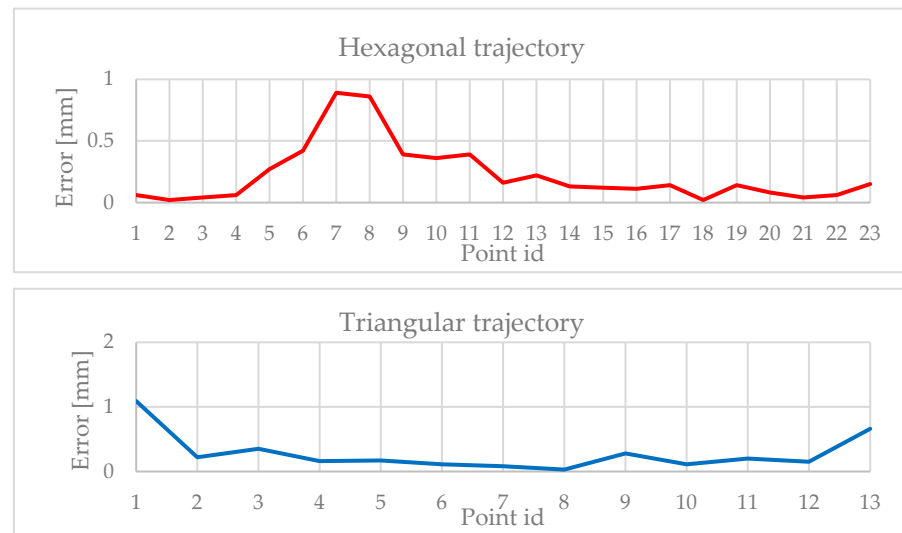


**Figure 15.** The hexagonal trajectory test shows a maximum error of almost 1 mm in a confined zone, while in the rest of the trajectory, the error is less than 0.2 mm. The triangular trajectory test shows similar maximum and minimum values for the errors.

#### 4. Discussion and Conclusions

The manipulator responds well to positioning in a large part of the working volume, but there is a confined area where the error is considerably larger. In the area where the error is small, this is lower than the prediction based on the error detected for the single

actuator. This is because the synergy between the three actuators ensures that the errors due to oscillations detected for the single actuator are dampened, reducing the error of the manipulator compared to what can be predicted based on a composition of the errors characterizing the individual actuators (Figure 11).

As for the area in which the error is most significant, it is clear that this derives from a discrepancy in the functioning of actuator number 2 compared to the others, which presents a more intense action than it should. It turns out that the positioning brings the end effector closer to the attack of actuator 2 than it should. This effect is noticeable in both trajectory tests.

Regarding the causes of this behavior, different lengths at rest can lead to this problem. Still, the authors believe that this problem has a limited effect, given that particular care was taken in constructing the actuators.

Another possible cause, and more probable than the first, is that actuator number 2 responds differently than the others due to the physical composition of the alloy and that it needs a slightly different electrical resistance deformation model from the one implemented for all three actuators. A possibility that should, therefore, be investigated in the future is the characterization of the actuators one by one, equipping each with a strain-electric resistance model to implement the sensor effect.

Another possibility could be to calibrate the system in the area where the errors are most significant and create a lookup table that can make corrections to increase precision.

To provide evidence of the advantages of the proposed device, a comparison was carried out with a similar device. The comparison was based on the number of DOFs, working volume, the accuracy in the positioning, the overall dimensions, the actuator's block control volume, and the mass. Figure 16 shows the considered device, and Table 3 compares the proposed device with the other under study.

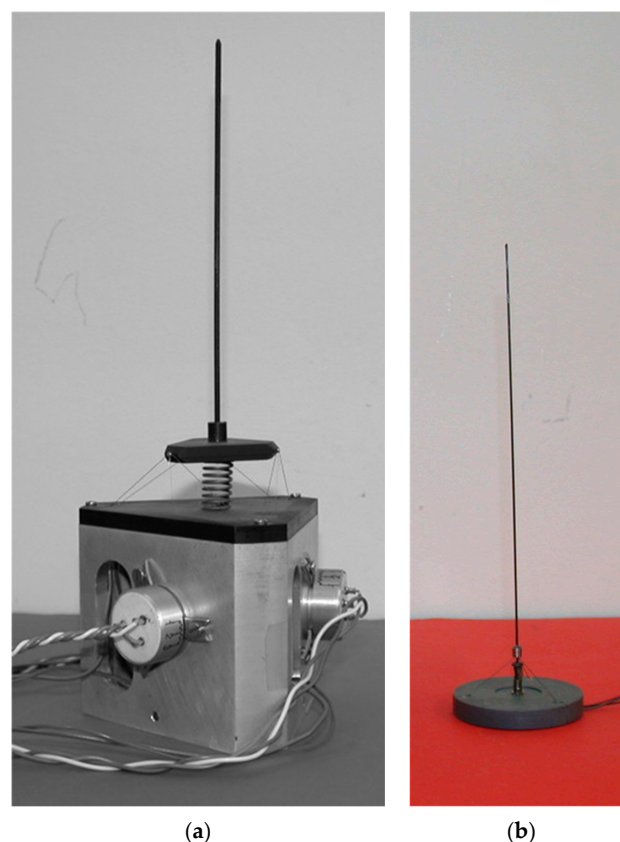


**Figure 16.** The manipulator used for comparison with the proposed device: (a) parallel manipulator with three DOFs actuated by Ni-Ti wires and controlled by the use of potentiometers [38]; (b) the proposed manipulator.



**Table 3.** Characteristics of the devices under comparison. DOFs = degrees of freedom; WV = working volume dimensions as diameter of the circle circumscribed to the shape of the WV in plant by height [mm × mm]; PA = typical positioning accuracy [mm]; OD = overall dimensions intended as diameter by height of the smaller cylinder containing the device [mm × mm]; ABV = actuator's block control volume [mm<sup>3</sup>]; M = mass of the device without electronics for control [kg]. Brackets (a)–(b) correspond to the devices shown in Figure 15; (c) represent the reference requirements.

Device	DOFs	WV	PA	OD	ABV	M
(a)	3	12 × 2	0.3	82 × 207	138,600	0.245
(b)	3	12 × 1.3	1/0.3	40.8 × 120	7844	0.012
(c)	3	10 × 2	0.1	45 × 140	20,000	0.050

From the comparison results, concerning the compared device, the proposed one has a smaller score just for the height of the working volume, with a result of about 66% of the compared one and a lower accuracy due to the problem of the malfunctioning of the actuator number 2, as discussed above. In all the other indices, the proposed device outperforms the compared one. From the comparison, it can be concluded that the proposed device has a better score for the requirements considered.

In [41], a study was carried out by the authors on an SMA wire actuator aimed at verifying the best controller with proportional (P), derivative (D), or integral (I) components or their combinations. In the future, the optimized controller will be implemented in the manipulator in question in order to verify possible improvements for the position accuracy.

Although the manipulator can move on spatial trajectories, the experimental trajectory tracking tests only involved flat trajectories in the horizontal plane. This is because having a setup for the survey and documentation of three-dimensional trajectories is not easy. The problem is difficult to solve given the small size of the working volume. A procedure that uses a small marker to be detected using a stereo camera is currently being studied. This study will constitute a future development of the present work.

**Author Contributions:** Conceptualization, F.D.; methodology, F.D., P.B.Z. and T.R.; validation, F.D.; formal analysis, F.D., P.B.Z. and T.R.; investigation, F.D., P.B.Z. and T.R.; data curation, F.D.; writing—original draft preparation, F.D.; writing—review and editing, F.D.; visualization, F.D., P.B.Z. and T.R.; supervision F.D., P.B.Z. and T.R. All authors have read and agreed to the published version of the manuscript.

**Funding:** This research received no external funding.

**Data Availability Statement:** Data are contained within the article.

**Acknowledgments:** The authors gratefully acknowledge the contribution of Emiliano Valentini in the experimental test reported in this paper.

**Conflicts of Interest:** The authors declare no conflicts of interest.

## References

1. Kittinanthapanya, R.; Sugahara, Y.; Matsuura, D.; Takeda, Y. Development of a Novel SMA-Driven Compliant Rotary Actuator Based on a Double Helical Structure. *Robotics* **2019**, *8*, 12. [CrossRef]
2. Britz, R.; Motzki, P.; Seelecke, S. Scalable Bi-Directional SMA-Based Rotational Actuator. *Actuators* **2019**, *8*, 60. [CrossRef]
3. Copaci, D.; Blanco, D.; Moreno, L. Flexible Shape-Memory Alloy-Based Actuator: Mechanical Design Optimization According to Application. *Actuators* **2019**, *8*, 63. [CrossRef]
4. Schmelter, T.; Theren, B.; Fuchs, S.; Kuhlenkötter, B. Development of an Actuator for Translatory Movement by Means of a Detented Switching Shaft Based on a Shape Memory Alloy Wire for Repeatable Mechanical Positioning. *Crystals* **2021**, *11*, 163. [CrossRef]
5. Ballester, C.; Copaci, D.; Arias, J.; Moreno, L.; Blanco, D. Hoist-Based Shape Memory Alloy Actuator with Multiple Wires for High-Displacement Applications. *Actuators* **2023**, *12*, 159. [CrossRef]
6. Dauksher, R.; Patterson, Z.; Majidi, C. Characterization and Analysis of a Flexural Shape Memory Alloy Actuator. *Actuators* **2021**, *10*, 202. [CrossRef]

7. Ameduri, S.; Concilio, A.; Favaloro, N.; Pellone, L. A Shape Memory Alloy Application for Compact Unmanned Aerial Vehicles. *Aerospace* **2016**, *3*, 16. [[CrossRef](#)]
8. Bovesecchi, G.; Corasaniti, S.; Costanza, G.; Tata, M. A Novel Self-Deployable Solar Sail System Activated by Shape Memory Alloys. *Aerospace* **2019**, *6*, 78. [[CrossRef](#)]
9. Liu, M.; Wang, Z.; Ikeuchi, D.; Fu, J.; Wu, X. Design and Simulation of a Flexible Bending Actuator for Solar Sail Attitude Control. *Aerospace* **2021**, *8*, 372. [[CrossRef](#)]
10. Costanza, G.; Delle Monache, G.; Tata, M.; Filosi, S. Development of SMA Spring Linear Actuator for an Autonomous Lock and Release Mechanism: Application for the Gravity-Assisted Pointing System in Moon to Earth Alignment of Directional Devices. *Aerospace* **2022**, *9*, 735. [[CrossRef](#)]
11. Dimino, I.; Vendittozzi, C.; Reis Silva, W.; Ameduri, S.; Concilio, A. A Morphing Deployable Mechanism for Re-Entry Capsule Aeroshell. *Appl. Sci.* **2023**, *13*, 2783. [[CrossRef](#)]
12. Braun, D.; Weik, D.; Elsner, S.; Hunger, S.; Werner, M.; Drossel, W. Position Control and Force Estimation Method for Surgical Forceps Using SMA Actuators and Sensors. *Materials* **2021**, *14*, 5111. [[CrossRef](#)] [[PubMed](#)]
13. Kim, H.; Jang, S.; Do, P.; Lee, C.; Ahn, B.; Kwon, S.; Chang, H.; Kim, Y. Development of Wearable Finger Prosthesis with Pneumatic Actuator for Patients with Partial Amputations. *Actuators* **2023**, *12*, 434. [[CrossRef](#)]
14. Deng, E.; Tadesse, Y. A Soft 3D-Printed Robotic Hand Actuated by Coiled SMA. *Actuators* **2021**, *10*, 6. [[CrossRef](#)]
15. Kotb, Y.; Elgamal, I.; Serry, M. Shape Memory Alloy Capsule Micropump for Drug Delivery Applications. *Micromachines* **2021**, *12*, 520. [[CrossRef](#)] [[PubMed](#)]
16. Shen, J.; Chen, Y.; Sawada, H. A Wearable Assistive Device for Blind Pedestrians Using Real-Time Object Detection and Tactile Presentation. *Sensors* **2022**, *22*, 4537. [[CrossRef](#)] [[PubMed](#)]
17. Copaci, D.; Serrano, D.; Moreno, L.; Blanco, D. A High-Level Control Algorithm Based on sEMG Signalling for an Elbow Joint SMA Exoskeleton. *Sensors* **2018**, *18*, 2522. [[CrossRef](#)] [[PubMed](#)]
18. He, J.; Lu, Y.; Wang, L.; Ma, N. On the Improvement of Thermal Protection for Temperature-Responsive Protective Clothing Incorporated with Shape Memory Alloy. *Materials* **2018**, *11*, 1932. [[CrossRef](#)] [[PubMed](#)]
19. Srivastava, R.; Alsamhi, S.; Murray, N.; Devine, D. Shape Memory Alloy-Based Wearables: A Review, and Conceptual Frameworks on HCI and HRI in Industry 4.0. *Sensors* **2022**, *22*, 6802. [[CrossRef](#)]
20. Lee, J.; Han, M. Design and Evaluation of Smart Textile Actuator with Chain Structure. *Materials* **2023**, *16*, 5517. [[CrossRef](#)]
21. Helps, T.; Vivek, A.; Rossiter, J. Characterization and Lubrication of Tube-Guided Shape-Memory Alloy Actuators for Smart Textiles. *Robotics* **2019**, *8*, 94. [[CrossRef](#)]
22. Raparelli, T.; Zobel, P.B.; Durante, F. A proposed methodology for the development of microgrippers: An application to a silicon device actuated by shape memory alloy wires. *Int. J. Mech. Eng. Technol.* **2018**, *9*, 235–249.
23. Zainal, M.; Sahlan, S.; Ali, M. Micromachined Shape-Memory-Alloy Microactuators and Their Application in Biomedical Devices. *Micromachines* **2015**, *6*, 879–901. [[CrossRef](#)]
24. Garcés-Schröder, M.; Hecht, L.; Vierheller, A.; Leester-Schädel, M.; Böhl, M.; Dietzel, A. Micro-Grippers with Femtosecond-Laser Machined In-Plane Agonist-Antagonist SMA Actuators Integrated on Wafer-Level by Galvanic Riveting. *Proceedings* **2017**, *1*, 385. [[CrossRef](#)]
25. Subendran, S.; Kang, C.; Chen, C. Comprehensive Hydrodynamic Investigation of Zebrafish Tail Beats in a Microfluidic Device with a Shape Memory Alloy. *Micromachines* **2021**, *12*, 68. [[CrossRef](#)]
26. Maffiodo, D.; Raparelli, T. Flexible Fingers Based on Shape Memory Alloy Actuated Modules. *Machines* **2019**, *7*, 40. [[CrossRef](#)]
27. Zeng, X.; Wu, Y.; Han, S.; Liu, Y.; Xiu, H.; Tian, F.; Ren, L. Theoretical and Experimental Investigations into a Crawling Robot Propelled by Piezoelectric Material. *Micromachines* **2021**, *12*, 1577. [[CrossRef](#)]
28. Perez-Sanchez, V.; Garcia-Rubiales, F.; Nekoo, S.; Arrue, B.; Ollero, A. Modeling and Application of an SMA-Actuated Lightweight Human-Inspired Gripper for Aerial Manipulation. *Machines* **2023**, *11*, 859. [[CrossRef](#)]
29. Raparelli, T.; Beomonte Zobel, P.; Durante, F. Mechanical design of a 3-dof parallel robot actuated by smart wires. In Proceedings of the EUCOMES 2008—The 2nd European Conference on Mechanism Science, Cassino, Italy, 17–20 September 2008; Springer: Dordrecht, The Netherlands, 2009; pp. 271–278. [[CrossRef](#)]
30. Shin, J.; Han, Y.; Lee, J.; Han, M. Shape Memory Alloys in Textile Platform: Smart Textile-Composite Actuator and Its Application to Soft Grippers. *Sensors* **2023**, *23*, 1518. [[CrossRef](#)]
31. Shi, L.; Guo, S.; Li, M.; Mao, S.; Xiao, N.; Gao, B.; Song, Z.; Asaka, K. A Novel Soft Biomimetic Microrobot with Two Motion Attitudes. *Sensors* **2012**, *12*, 16732–16758. [[CrossRef](#)]
32. Rajagopalan, R.; Petruska, A.; Howard, D. A Bi-State Shape Memory Material Composite Soft Actuator. *Actuators* **2022**, *11*, 86. [[CrossRef](#)]
33. Sreekumar, M.; Singaperumal, M.; Nagarajan, T.; Zoppi, M.; Molfino, R. A compliant miniature parallel manipulator with shape memory alloy actuators. In Proceedings of the IEEE International Conference on Industrial Technology, Mumbai, India, 15–17 December 2006; pp. 848–853. [[CrossRef](#)]
34. Elwaleed, A.K.; Mohamed, N.A.; Nor, M.J.M.; Mustafa, M.M. A new method for actuating parallel manipulators. *Sens. Actuators A Phys.* **2008**, *147*, 593–599. [[CrossRef](#)]
35. Giuseppe, C. Experimental characterization of a binary actuated parallel manipulator. *Chin. J. Mech. Eng.* **2016**, *29*, 445–453. [[CrossRef](#)]

36. AbuZaiter, A.; Ng, E.L.; Kazi, S.; Mohamed Ali, M.S. Development of Miniature Stewart Platform Using TiNiCu Shape-Memory-Alloy Actuators. *Adv. Mater. Sci. Eng.* **2015**, *2015*, 928139. [[CrossRef](#)]
37. Ranjith Pillai, R.; Ganesan, M. Mechatronics Design and Kinematic Analysis of SMA Spring Actuated Parallel Manipulator. *J. Phys. Conf. Ser.* **2021**, *1969*, 012011. [[CrossRef](#)]
38. Raparelli, T.; Zobel, P.B.; Durante, F. Design of a parallel robot actuated by shape memory alloy wires. *Mater. Trans.* **2002**, *43*, 1015–1022. [[CrossRef](#)]
39. Landsberger, S.E.; Sheridan, T.B. A minimal, minimal linkage: The tension-compression parallel link manipulator. In Proceedings of the IMACS/SICE International Symposium on Robotics, Mechatronics, and Manufacturing Systems, Kobe, Japan, 16–20 September 1992; pp. 493–500.
40. Raparelli, T.; Beomonte Zobel, P.; Durante, F. A robot actuated by shape memory alloy wires. In Proceedings of the Industrial Electronics, 2002. ISIE 2002, Proceedings of the 2002 IEEE International Symposium on, L'Aquila, Italy, 8–11 July 2002; IEEE: Piscataway, NJ, USA, 2002; Volume 2, pp. 420–423. [[CrossRef](#)]
41. Durante, F.; Raparelli, T.; Beomonte Zobel, P. Resistance Feedback of a Ni-Ti Alloy Actuator at Room Temperature in Still Air. *Micromachines* **2024**, *15*, 545. [[CrossRef](#)] [[PubMed](#)]
42. Gosselin, C.; Angeles, J. Singularity Analysis of Closed-Loop Kinematic Chains. *IEEE Trans. Robot. Autom.* **1990**, *6*, 281–290. [[CrossRef](#)]

**Disclaimer/Publisher's Note:** The statements, opinions and data contained in all publications are solely those of the individual author(s) and contributor(s) and not of MDPI and/or the editor(s). MDPI and/or the editor(s) disclaim responsibility for any injury to people or property resulting from any ideas, methods, instructions or products referred to in the content.